

Substrate-supported triplet superconductivity in Dirac semimetals

Domenico Di Sante^{†,1} Xianxin Wu^{†,1} Mario Fink,¹ Werner Hanke,¹ and Ronny Thomale¹

¹*Institut für Theoretische Physik und Astrophysik, Universität Würzburg,
Am Hubland Campus Süd, Würzburg 97074, Germany**

(Dated: September 12, 2018)

Stimulated by the success of graphene and its emerging Dirac physics [1], the quest for versatile and tunable electronic properties in atomically thin systems has led to the discovery of various chemical classes of 2D compounds [2]. In particular, honeycomb lattices of group-IV elements, such as silicene and germanene, have been found experimentally [3–7]. Whether it is a necessity of synthesis or a desired feature for application purposes, most 2D materials demand a supporting substrate. In this work, we highlight the constructive impact of substrates to enable the realization of exotic electronic quantum states of matter, where the buckling emerges as the decisive material parameter adjustable by the substrate. At the example of germanene deposited on MoS₂, we find that the coupling between the monolayer and the substrate, together with the buckled hexagonal geometry, conspire to provide a highly suited scenario for unconventional triplet superconductivity upon adatom-assisted doping.

Material synthesis in two spatial dimensions is one of the rising fields of contemporary condensed matter physics. Initiated by the exfoliation and substrate-assisted growth of graphene [8], complementary techniques such as refined sputtering and molecular beam epitaxy are significantly broadening the scope of 2D material classes, which by themselves are considered promising hosts for exotic electronic quantum states of matter. This includes not only topological quantum matter such as quantum spin Hall (QSH) insulators and Chern insulators [9, 10], but also unconventional superconductors, which has recently climaxed in the discovery of superconductivity in doped twisted bilayer graphene [11].

For 2D superconductors, an overarching principle is to attempt to access high density of states (DOS) at the Fermi level which constitutes a promising setup for high critical temperatures. For graphene, at a filling factor corresponding to $\sim 13\%$ of doping concentration, a van Hove singularity (vHs) in the DOS was proposed to drive a substantial enhancement of interaction effects [12]. One striking consequence is the predicted appearance of $d + id$ -wave superconductivity [13–15], which would allow to enter the rich phenomenology of topological superconductors. Several attempts have been made to dope graphene to the vH point by chemical doping [16]. Notwithstanding the efforts, so far no evidence for the observation of unconventional superconductivity has been reported. This is presumably because of the added disorder capping the large DOS at the vHs, which, in graphene, only shows up (see Fig. 1) at energies, away from the Fermi level at half-filling, comparable to the nearest-neighbor hopping parameter (~ 3 eV). As a consequence, one guiding principle for improve-

ment is to identify alternative scenarios in which vHs filling can be achieved at lower doping.

Silicene and germanene as 2D-Xenes exhibit larger bond lengths than graphene and prevent the atoms from forming strong π -bonds, yielding a smaller nearest-neighbor hopping (~ 1 eV). The growth of such systems requires proper substrates and templates. Aiming at QSH insulator phases, 2D-Xenes may be suited because of their heavy constituent atoms and the larger spin-orbit mediated topological band gap [17–19]. X-ene geometric reconstruction has been reported for metallic substrates Ag, Au, Pt, Al and Ir [3–5], as well as less interacting substrates as MoS₂ and AlN [6, 7]. Common reconstructed phases are $\sqrt{3} \times \sqrt{3}$, $\sqrt{7} \times \sqrt{7}$, 2×2 , but also the larger 3×3 and 5×5 setting [2]. Bonding with the substrate and complex surface reconstructions render the analysis of realistic systems a challenging task from experiment and theory. Furthermore, the strong monolayer/substrate interaction often avoids the QSH scenario in favour of, on a first view, an undesirable metallic phase [7, 20]. In light of unconventional superconductivity, however, the key insight of our work is that the presence of a substrate can drastically modify the low-energy physics of 2D-Xenes in an advantageous manner, as to create a new fermiology characterized by enlarged DOS already at pristine filling, and a vHs accessible upon moderate doping. As the graphene-type fermiology is fundamentally altered through the substrate, we find that substrate-supported 2D electronic structures establish an intriguing platform for unconventional Fermi surface instabilities in general, and superconductivity in particular. By germanene on MoS₂, we identify an electronic structure which promises to be preeminent suited for the observation of f -wave superconductivity, a state which has so far remained elusive in nature.

The peculiar properties of Ge/MoS₂ already become visible from a comparison of DOS against graphene (Fig. 1). Already at half filling, Ge/MoS₂ exhibits a sizable carrier density. Even more remarkably, however, the vHs, in particular the one on the electron-doped side, is shifted closer to half filling as compared to graphene. This observation is of general importance independent of the type of Fermi surface instability we are interested in, since all instability scales, from the viewpoint of weak coupling, are enhanced by an enlarged DOS at the Fermi level. As a next step, we analyze the detailed fermiology and general microscopic setting of Ge/MoS₂ in the vicinity of vH filling.

Fig. 2a shows the established structural model for 5×5 germanene on 6×6 MoS₂ [7], while in Table I and in the Supplementary Information we also report the cases of 3×3 germanene on 4×4 AlN/Ag(111) [6] and $\sqrt{3} \times \sqrt{3}R(30^\circ)$

TABLE I: **Structural and hopping parameters in the 8-bands NN Slater-Koster tight-binding model.** Δ_3 (Å) is the buckling parameter of the honeycomb lattice (see Fig. 2a), described also by the buckling angle θ ($^\circ$) between the Ge-Ge bond and the z direction normal to the surface. ϵ_s , $\epsilon_{p_{x,y}}$ and ϵ_{p_z} (eV) are the on-site energies of the s , p_x , p_y and p_z orbitals, while $V_{ss\sigma}$, $V_{sp\sigma}$, $V_{pp\sigma}$ and $V_{pp\pi}$ (eV) parametrize the Slater-Koster transfer integrals. DS, CDS and M in the last column are acronym for Dirac Semimetal, Compensated Dirac Semimetal and Metallic phases of the ground state, respectively. The bandstructures for Ge/AlN/Ag(111) and Ge/Au(111) are shown in the Supplementary Information.

	reconstruction	Δ_3	θ	ϵ_s	$\epsilon_{p_{x,y}}$	ϵ_{p_z}	$V_{ss\sigma}$	$V_{sp\sigma}$	$V_{pp\sigma}$	$V_{pp\pi}$	phase
Ge/AlN/Ag(111)	$3 \times 3/4 \times 4$	0.70	107.3	-5.44	2.76	0.86	-1.8	2.5	3.3	-1.0	DS
Ge/MoS ₂	$5 \times 5/6 \times 6$	0.86	111.4	-5.74	2.46	0.56	-2.0	2.5	3.3	-1.2	CDS
Ge/Au(111)	$\sqrt{3} \times \sqrt{3}/\sqrt{7} \times \sqrt{7}$	0.47	100.5	-6.24	1.96	0.06	-1.5	2.5	3.3	-1.2	M

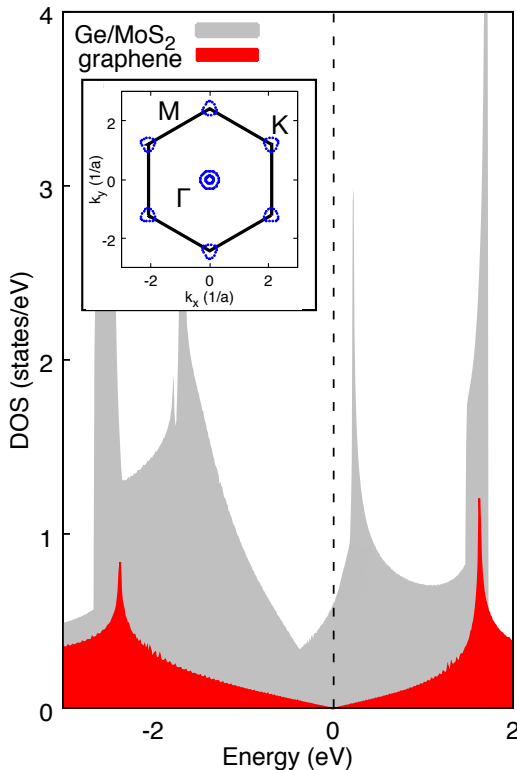


FIG. 1: **Fermi surface and density of the states.** Comparison between the DOS of graphene (red) and germanene/MoS₂ (grey). The Fermi level, corresponding to the vertical dashed line, is set to half-filling in both cases, and separates the hole doping (left) from the electron doping (right) regimes. The inset shows the Fermi surface of germanene/MoS₂ in the absence of doping.

germanene on $\sqrt{7} \times \sqrt{7}R(19.1^\circ)$ Au(111) [5]. We computed the supercell's bandstructure and unfolded it into the primitive Brillouin zone, obtaining the unfolding weights (red symbols in Fig. 2b, see Methods for references). When grown on MoS₂, the electronic states of germanene are weakly disturbed by the interaction with the substrate. The significant compressive lateral strain on the honeycomb lattice ($\sim 5\%$), however, increases the buckling distortion up to 0.86 Å, and induces a crossing of the Fermi level around the Γ point by hole-like bands (see also the Supplementary Information), turning the system into a compensated Dirac semimetal phase with a finite DOS at the Fermi level. We develop a realistic tight-

binding model able to reproduce the single particle bandstructure of Ge/MoS₂ [21]. In Table I, we report our parameter fit to the ab initio results within a simplified nearest-neighbour (NN) approximation (Fig. 2c for Ge/MoS₂). Next-nearest-neighbor hoppings are delegated to the Supplementary Information; as another step of refinement, instead of resorting to a tight-binding fit, we also employ a full Wannier function based model, which we have used for our Fermi surface instability calculations.

In graphene, 0.5 electron doping per unit cell is needed to reach the vHs point. At the present stage of experimental capabilities, such a high electron doping is unavoidably accompanied by detrimental disorder effects. In Ge/MoS₂, as the vHs point is energetically closer to the Fermi level, the vHs can be reached upon doping of ~ 0.2 electrons per unit cell, i.e., only 40% of the doping value needed for graphene. In Fig. 2b, we show the bandstructure of Ge/MoS₂ upon doping by 3 alkali atoms per unit cell. This doping shifts the vHs close to the Fermi level (without much affecting the states around the Γ point) by providing 0.12 electrons, such that the vHs now is only 0.1 eV above the Fermi level.

The Fermi surface of Ge/MoS₂ doped to the vHs is shown in Fig. 3a. It is almost circular and rather flat along the $M - K$ line, which is in sharp contrast to the expected hexagonal shape for vH-doped graphene. In graphene, the nesting between opposite edges of the hexagonal Fermi surface promotes strong antiferromagnetic fluctuations around the M point, which in turn drive the $d + id$ pairing states [13–15]. In Ge/MoS₂, this nesting is absent due to the circular Fermi surface, and the dominant nesting (denoted by the arrow) promotes ferromagnetic fluctuations. This is evident from the intense $\mathbf{q} = 0$ peak in the momentum space distribution of the bare susceptibility shown in Fig. 3b. Furthermore, the Fermi velocities of graphene and Ge/MoS₂ are different. For the former, the minimum of the Fermi velocity is localized around the M point, leading to a peaked DOS in its vicinity. For the latter, a high DOS is extended over a large fraction of the Fermi surface (see Fig. 3a), and any minimal reduction to the M points is no longer valid [13].

We adopt the functional renormalization group (FRG) approach to study the Fermi surface instabilities, by starting from the bare many-body interaction and integrating out the high-energy degrees of freedom [22, 23]. The renormalized interaction $V_\Lambda(\mathbf{k}_1, \mathbf{k}_2, \mathbf{k}_3, \mathbf{k}_4)$ described by the 4-point

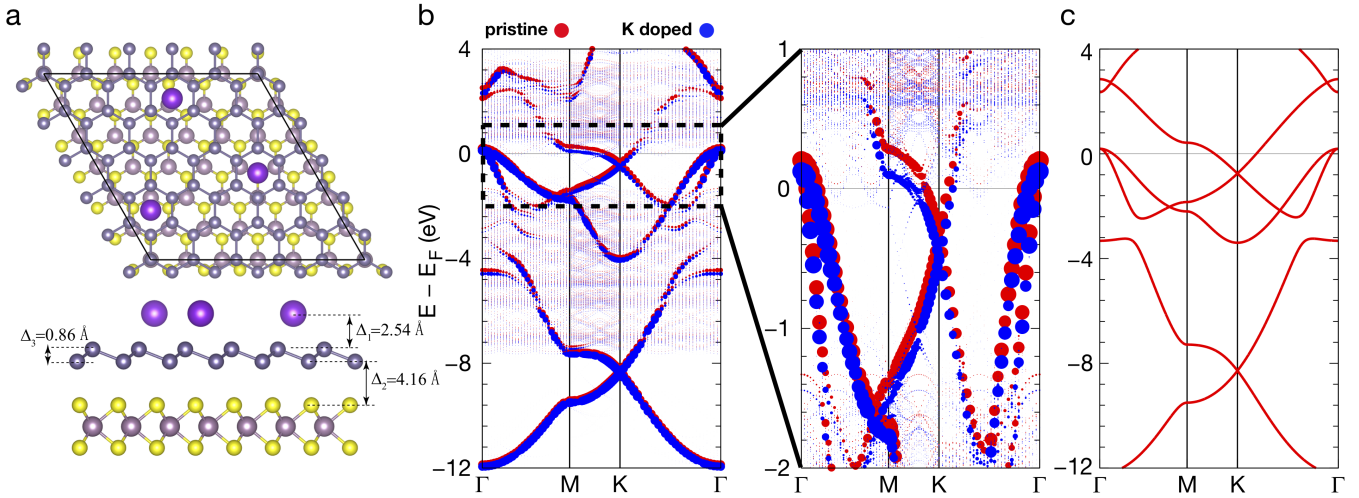


FIG. 2: **First-principles calculations of realistic germanene/MoS₂.** **a** Structural model for 5×5 germanene on 6×6 MoS₂, with the inclusion of potassium atoms to simulate chemical doping. **b** DFT bandstructure (wide energy range view on the left and zoom around the Fermi level on the right) of the superstructure in panel **a** along the high-symmetry-lines of the 1×1 Brillouin zone. The red and blue circles highlight the weights of the unfolded electronic states for the pristine and K-doped system, respectively. **c** Bandstructure of the nearest-neighbour tight-binding (TB) Slater-Koster model with parameters listed in Table I and Hamiltonian given in the Methods section.

function (4PF) diverges in some channels as the cutoff Λ approaches the Fermi surface, marking the onset of a leading instability (see Methods). The parameterization of germanene on MoS₂ (bandwidth $W \sim 20$ eV) serves as the non-renormalized limit for our FRG study. The interaction Hamiltonian we consider contains intra- and inter-orbital repulsion U and U' , as well as Hund's rule coupling J and pair-hopping J' (see Methods). For simplicity, in the absence of ab-initio estimates of the interaction parameters, we choose the ansatz $U = U' + 2J$, $U = 2U'$, and $J = J'$, tuning the global scale such that the resulting maximum strength of the initial vertex function $V_{\Lambda=W}(\mathbf{k}_1, \mathbf{k}_2, \mathbf{k}_3, \mathbf{k}_4)$ for momenta on the Fermi surface is still located in the weak to intermediate coupling regime. We use the same Hamiltonian within a multiband random phase approximation (RPA) fluctuation exchange approximation scheme [24] in order to provide an independent

validation of our FRG results. Note that spin-orbit coupling (SOC) has not been taken into account, which promotes a more efficient implementation. This assumption is justified for germanene: as a recent theoretical study demonstrates, in Ge/MoS₂ the layer/substrate interaction sensibly reduces the influence of SOC compared to the freestanding case [25].

Near the vHs, we find a prominent superconducting instability in the spin triplet sector, since the renormalized vertex V_{Λ} diverges in this channel as Λ approaches the FRG flow the Fermi level (see Fig. 4a). The leading pairing state transforms according to the A_{1u} irreducible representation of D_{3d} , i.e., the point group symmetry of the buckled geometry of germanene. Imposing a mean field decoupling in the diverging vertex channel [26], we find that the gap function $\Delta_{\mathbf{k}}$ associated to the leading instability shows a $f_{y(y^2-3x^2)}$ profile, where the gap function changes sign every 60° rotation and has line nodes along the $k_y = 0$, $k_y = \pm\sqrt{3}k_x$ lines (see Fig. 4b). The FRG results are validated by RPA fluctuation exchange calculations, the results of which we show in Fig. 4c, where we also find the dominant pairing state to be located in the A_{1u} lattice group representation (see Methods section for details). As the Fermi pocket is rather circular and does not exhibit a particularly peaked momentum structure of the DOS at the Fermi level, the $\mathbf{q} = 0$ particle-hole fluctuation channel is dominant. This naturally promotes the tendency towards triplet pairing, where all sub-channels satisfy the condition that the gap function connected by the nesting vector \mathbf{q} (see Fig. 3a) must have the same sign. This is a recurrent motif from other theoretical proposals for f -wave superconductivity, such as employing the sublattice interference in a kagome metal [27].

Within the triplet channel, microscopic details such as the hexagonal symmetry then yield a preference of the f -wave

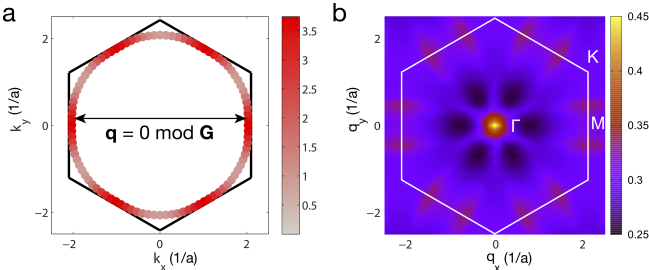


FIG. 3: **Fermiology of germanene/MoS₂ at vHs point.** **a** Fermi surface and momentum distribution of the DOS ($\rho_{\mathbf{k}} \sim 1/|v_F(\mathbf{k})|$, with $v_F(\mathbf{k})$ the Fermi velocity) at the vHs energy. The arrow highlights the $\mathbf{q} = 0$ nesting vector up to a reciprocal lattice vector. **b** Momentum distribution of the RPA bare susceptibility (see Methods). The color bars are in eV Å and eV⁻¹ units, respectively.

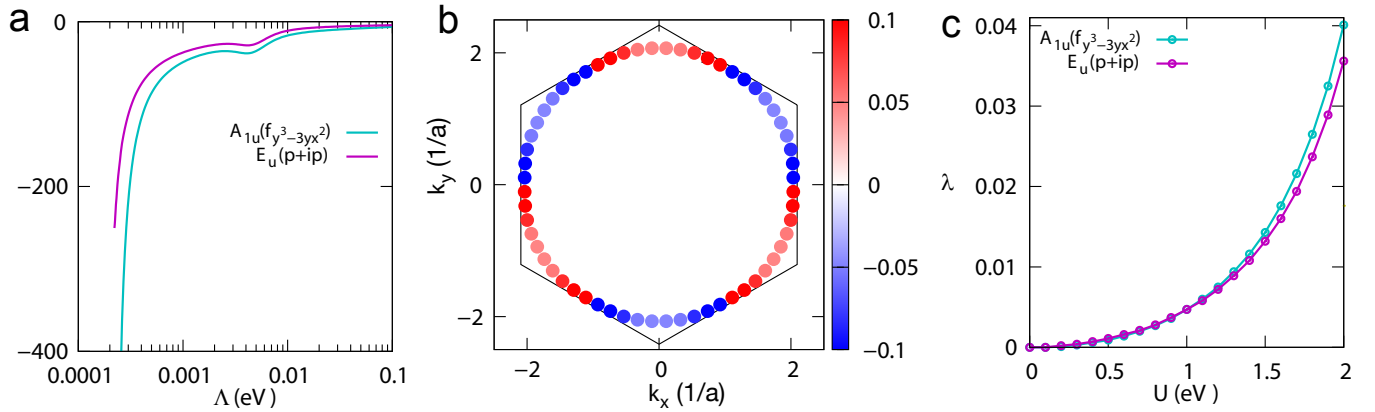


FIG. 4: **Superconducting instability.** **a** Typical FRG flow of the Fermi surface instabilities when the chemical potential is set slightly below the vHs as a function of the infrared cutoff Λ ($\max|V_{\Lambda=W}(\mathbf{k}_1, \mathbf{k}_2, \mathbf{k}_3, \mathbf{k}_4)| = 2.0$ eV). The superconducting channels of the mean-field decomposition are labelled according the irreducible representations of D_{3d} they transform to. **b** Modulation of the superconducting gap of the leading f -wave instability along the Fermi surface (arb. units). **c** Typical RPA results at the vHs as a function of the intra-orbital repulsion U at fixed $J/U = 0.2$ ratio. λ s are the eigenvalues of the RPA pairing vertex (see Methods).

state over other candidates states such as the p -wave state, which is the subleading instability both at the FRG and RPA level. We also note that the competition between the f - and p -wave instability can to some extent be tuned by varying the J/U ratio in the interaction Hamiltonian. This is an interesting perspective if we assume that the Hund's coupling can be tailored by substrate engineering. The agreement between FRG and RPA significantly supports the prediction of f -wave triplet superconductivity in Ge/MoS₂. This is because it might sometimes occur that the relevance of ferromagnetic fluctuations is overestimated. At the instance of LiFeAs, early RPA studies had predicted p -wave superconductivity [28], whereas FRG found a dominant extended s -wave which agreed with the finally converging picture from experimental evidence [29].

Our combined ab initio, RPA, and FRG analysis points out that the recently synthesized 2D-Xene Ge/MoS₂ is a promising platform for studying unconventional Fermi surface instabilities, in light of triplet superconductivity. In order to reach the scenario outlined here, further steps of experimental refinement suggest themselves to be followed up on. First, there appears to be an electronic level mismatch between the current Ge/MoS₂ in experiment and the ab initio simulations, possibly due to non-saturated defects [7]. Second, to avoid detrimental disorder effects from chemical doping, one might want to pursue electrostatic doping from gating methods. Recent experiments have achieved a doping in MoS₂ of $\sim 1.2 \times 10^{14}$ cm⁻² carrier density [30], which, if transferred to germanene, would correspond to ~ 0.08 electrons. At this doping level, our calculations already suggest a propensity towards a $f_{x(x^2-3y^2)}$ -wave instability, even though higher doping would still be desirable. From a broader perspective, this is only the beginning to employ *substrate engineering* towards accomplishing exotic Fermi surface instabilities. As significant progress has already been made at the frontier of

substrate-assisted topological insulators [19], we hope that our work will stimulate similar efforts for unconventional superconductivity in layer/substrate heterostructures.

Methods

The model. The eight-band tight binding model with a simple nearest neighbor hopping parameterization for germanene is given by

$$H_0 = \sum_{\alpha\beta} \sum_{\mu\nu\sigma} h_{\mu\nu}^{\alpha\beta}(\mathbf{k}) c_{\alpha\mu\sigma}^{\dagger}(\mathbf{k}) c_{\beta\nu\sigma}(\mathbf{k}),$$

where $\alpha/\beta = A, B$ is the sublattice index and $\mu/\nu = 1, 2, 3, 4$ represent the s , p_z , p_x and p_y orbitals, respectively. $c_{\alpha\mu\sigma}^{\dagger}$ creates a spin σ electron in μ orbital on α sublattice with momentum \mathbf{k} . The matrix elements $h_{\mu\nu}^{\alpha\beta}(\mathbf{k})$ are given by,

$$\begin{aligned} h^{AA}(\mathbf{k}) &= h^{BB}(\mathbf{k}) = \text{diag}(\epsilon_s, \epsilon_{p_z}, \epsilon_{p_x}, \epsilon_{p_y}) \\ h_{11}^{AB}(\mathbf{k}) &= r^{11}(e^{ix} + 2e^{-\frac{ix}{2}} \cos y) \\ h_{22}^{AB}(\mathbf{k}) &= t^{11}(e^{ix} + 2e^{-\frac{ix}{2}} \cos y) \\ h_{12/21}^{AB}(\mathbf{k}) &= \pm s^{11}(e^{ix} + 2e^{-\frac{ix}{2}} \cos y) \\ h_{13/31}^{AB}(\mathbf{k}) &= \pm(s_1^{12}e^{ix} - s_1^{12}e^{-\frac{ix}{2}} \cos y) \\ h_{14/41}^{AB}(\mathbf{k}) &= \pm\sqrt{3}is_1^{12}e^{-\frac{ix}{2}} \sin y \\ h_{23/32}^{AB}(\mathbf{k}) &= t_1^{12}e^{ix} - t_1^{12}e^{-\frac{ix}{2}} \cos y \\ h_{24/42}^{AB}(\mathbf{k}) &= \sqrt{3}it_1^{12}e^{-\frac{ix}{2}} \sin y \\ h_{33}^{AB}(\mathbf{k}) &= t_{11}^{22}e^{ix} + \frac{1}{2}(t_{11}^{22} + 3t_{22}^{22})e^{-\frac{ix}{2}} \cos y \\ h_{34/43}^{AB}(\mathbf{k}) &= -\frac{\sqrt{3}i}{2}(t_{11}^{22} - t_{22}^{22})e^{-\frac{ix}{2}} \sin y \\ h_{44}^{AB}(\mathbf{k}) &= t_{22}^{22}e^{ix} + \frac{1}{2}(3t_{11}^{22} + t_{22}^{22})e^{-\frac{ix}{2}} \cos y \end{aligned}$$

where $x = k_x a_0 / \sqrt{3}$, $y = k_y a_0 / 2$, a_0 is the in-plane lattice constant, r represents hopping between $s - s$ orbitals, t represents hopping between $p - p$ orbitals and s represents hopping between $s - p$ orbitals. The hopping parameters in the model are,

$$\begin{aligned} r^{11} &= V_{ss\sigma} \\ t^{11} &= V_{pp\sigma} \cos^2 \theta + V_{pp\pi} \sin^2 \theta \\ s_1^{12} &= V_{sp\sigma} \sin \theta \\ s_1^{11} &= V_{sp\sigma} \cos \theta \\ t_1^{12} &= -(V_{pp\pi} - V_{pp\sigma}) \cos \theta \sin \theta \\ t_{11}^{22} &= V_{pp\sigma} \sin^2 \theta + V_{pp\pi} \cos^2 \theta \\ t_{22}^{22} &= V_{pp\pi} \end{aligned}$$

with θ and Slater-Koster parameters V listed in Table I of the main text. A more elaborated model which includes next-nearest-neighbour hopping terms is given in the Supplementary Information. For the actual FRG and RPA calculations shown in the main text we used an ab initio Hamiltonian based on Wannier Functions, which including long range hopping terms, gives the best description of the DFT bandstructure.

The interaction part of the Hamiltonian for the multi-orbital system considered here is

$$\begin{aligned} H_{int} = & U \sum_{i\alpha} n_{i\alpha\uparrow} n_{i\alpha\downarrow} + U' \sum_{i,\alpha<\beta} n_{i\alpha} n_{i\beta} + \\ & J \sum_{i,\alpha<\beta, \sigma\sigma'} c_{i\alpha\sigma}^\dagger c_{i\beta\sigma'}^\dagger c_{i\alpha\sigma'} c_{i\beta\sigma} + \\ & J' \sum_{i,\alpha\neq\beta} c_{i\alpha\uparrow}^\dagger c_{i\alpha\downarrow}^\dagger c_{i\beta\downarrow} c_{i\beta\uparrow} \end{aligned} \quad (1)$$

where $n_{i\alpha} = n_{\alpha\uparrow} + n_{\alpha\downarrow}$. U , U' , J and J' parametrize the intra- and inter-orbital repulsion, as well as the Hund's rule and pair-hopping terms, respectively.

DFT calculations. We employed first-principles calculations based on the density functional theory as implemented in the Vienna ab initio simulation package (VASP)[31], within the projector-augmented-plane-wave (PAW) method[32, 33]. The generalized gradient approximation as parametrized by the PBE-GGA functional for the exchange-correlation potential was used[34], by expanding the Kohn-Sham wavefunctions into plane-waves up to an energy cut-off of 600 eV, and we sampled the Brillouin zone on an $8 \times 8 \times 1$ regular mesh. The large structural reconstruction enforces a folding of the electronic states into the supercell Brillouin zones, which map onto the primitive 1×1 Brillouin zone. It is usually simpler to achieve a transparent physical description in the latter setting, where the unfolded bandstructure readily compares with the freestanding models when the symmetry breaking induced by the reconstruction is weak. The unfolding procedure we adopt in this work follows the lines described in Refs[35, 36].

FRG calculations. The basic idea of the functional Renormalization Group (FRG) method is similar to other RG concepts in that the "high-energy" degrees of freedom are thinned out while leaving the low-energy physics invariant. In this way, FRG has become a much-used general concept to derive effective theories, e.g. at long length scales or for a low-energy window. For weakly to intermediately coupled Fermion systems, one is mainly interested in the effective interactions near the Fermi surface (E_F), as they contain relevant information about possibly symmetry-broken (magnetic, superconducting, etc) and other non-Fermi-liquid ground states. Therefore, by systematically integrating out degrees of freedom, one can access competing orders at low-energy or temperature in the phase diagram[22, 23].

The RG approaches to interacting Fermions are less biased than diagrammatic summations in a particular channel, as competing fluctuations (magnetic, superconducting, screening, vertex corrections) are included on equal footing. This differs, in particular, from the random-phase-approximation (RPA) which, considering superconductivity, takes right from the outset a magnetically spin-fluctuation driven pairing interaction.

To compute the effective interactions near E_F , one typically uses the RG flow equations for the effective action, or, one-particle irreducible vertex functions[22, 23]. These schemes are named functional RG, as they aim at keeping as much as possible the wave vector dependence of the two-particle interaction $V_\Lambda(\mathbf{k}, \mathbf{p})$, where Λ denoted the RG flow parameter.

In the FRG one starts from the bare many-body interaction. The pairing is then "dynamically" generated by integrating out the high-energy degrees of freedom. For a given instability, characterized by the order parameter $\hat{O}_\mathbf{k}$, the 4-point function (4PF) $V_\Lambda(\mathbf{k}, \mathbf{p})$, in the particular ordering channel, can be written in shorthand notation as $\sum_{\mathbf{k}, \mathbf{p}} V_\Lambda(\mathbf{k}, \mathbf{p}) [\hat{O}_\mathbf{k}, \hat{O}_\mathbf{p}]$ [22, 23, 37]. Accordingly, the 4PF $V_\Lambda(\mathbf{k}_i - \mathbf{k}_j, \mathbf{p}_i - \mathbf{p}_j)$ in the Cooper channel can be decomposed into different contributions:

$$V_\Lambda^{\text{SC}}(\mathbf{k}, \mathbf{p}) = \sum_i c_i^{\text{SC}}(\Lambda) f_i^{\text{SC}*}(\mathbf{k}) f_i^{\text{SC}}(\mathbf{p}) \quad (2)$$

where i is a symmetry decomposition index. The leading instabilities of that channel then corresponds to an eigenvalue $c_i^{\text{SC}}(\Lambda)$ first diverging under the flow of Λ . $f_i^{\text{SC}}(\mathbf{k})$ is the superconducting form factor of the pairing mode i , which tells us about the superconducting pairing symmetry and, hence, gap structure associated with it. In the FRG scheme, from the final Cooper channel 4PF, this quantity is computed along the discretized Fermi surfaces (as shown in Fig. 4b), and the leading instabilities are plotted in Fig. 4a.

RPA fluctuation exchange calculations. We adopt the standard multi-orbital RPA approach[24, 38–41], with parameter notations given in Ref. 38. The bare susceptibility is de-

fine as

$$\chi_{l_1 l_2 l_3 l_4}^0(\mathbf{q}, \tau) = \frac{1}{N} \sum_{\mathbf{k} \mathbf{k}'} \langle T_\tau c_{l_3 \sigma}^\dagger(\mathbf{k} + \mathbf{q}, \tau) c_{l_4 \sigma}(\mathbf{k}, \tau) c_{l_2 \sigma}^\dagger(\mathbf{k}' - \mathbf{q}, 0) c_{l_1 \sigma}(\mathbf{k}', 0) \rangle_0. \quad (3)$$

where l_i is the orbital indices. The bare susceptibility in momentum-frequency space is then given by

$$\chi_{l_1 l_2 l_3 l_4}^0(\mathbf{q}, i\omega_n) = -\frac{1}{N} \sum_{\mathbf{k} \mu \nu} a_\mu^{l_4}(\mathbf{k}) a_\mu^{l_2*}(\mathbf{k}) a_\nu^{l_1}(\mathbf{k} + \mathbf{q}) \times a_\nu^{l_3*}(\mathbf{k} + \mathbf{q}) \frac{n_F(E_\mu(\mathbf{k})) - n_F(E_\nu(\mathbf{k} + \mathbf{q}))}{i\omega_n + E_\mu(\mathbf{k}) - E_\nu(\mathbf{k} + \mathbf{q})}, \quad (4)$$

where μ/ν is the band index, $n_F(\epsilon)$ is the Fermi distribution function, $a_\mu^{l_4}(\mathbf{k})$ is the l_4 -th component of the eigenvector for band μ resulting from the diagonalization of the single particle Hamiltonian H_0 and $E_\mu(\mathbf{k})$ is the corresponding eigenvalue. The interacting spin susceptibility and charge susceptibility at the RPA level are given by

$$\chi_1^{RPA}(\mathbf{q}) = [1 - \chi_0(\mathbf{q}) U^s]^{-1} \chi_0(\mathbf{q}), \quad (5)$$

$$\chi_0^{RPA}(\mathbf{q}) = [1 + \chi_0(\mathbf{q}) U^c]^{-1} \chi_0(\mathbf{q}), \quad (6)$$

where U^s, U^c are the interaction matrices:

$$U_{l_1 l_2 l_3 l_4}^s = \begin{cases} U & l_1 = l_2 = l_3 = l_4, \\ U' & l_1 = l_3 \neq l_2 = l_4, \\ J & l_1 = l_2 \neq l_3 = l_4, \\ J' & l_1 = l_4 \neq l_2 = l_3, \end{cases} \quad (7)$$

$$U_{l_1 l_2 l_3 l_4}^c = \begin{cases} U & l_1 = l_2 = l_3 = l_4, \\ -U' + 2J & l_1 = l_3 \neq l_2 = l_4, \\ 2U' - J & l_1 = l_2 \neq l_3 = l_4, \\ J' & l_1 = l_4 \neq l_2 = l_3, \end{cases} \quad (8)$$

The effective interaction within the RPA approximation is thus

$$V_{eff} = \sum_{ij, \mathbf{k} \mathbf{k}'} \Gamma_{ij}(\mathbf{k}, \mathbf{k}') c_{i\mathbf{k}\uparrow}^\dagger c_{i\mathbf{k}\downarrow}^\dagger c_{j\mathbf{k}'\downarrow} c_{j\mathbf{k}'\uparrow} \quad (9)$$

where the momenta \mathbf{k} and \mathbf{k}' are restricted to different FS C_i with $\mathbf{k} \in C_i$ and $\mathbf{k}' \in C_j$ and $\Gamma_{ij}(\mathbf{k}, \mathbf{k}')$ is the pairing scattering vertex in the singlet channel[38]. The pairing vertex is,

$$\Gamma_{ij}(\mathbf{k}, \mathbf{k}') = Re \left[\sum_{l_1 l_2 l_3 l_4} a_{v_i}^{l_2,*}(\mathbf{k}) a_{v_i}^{l_3,*}(-\mathbf{k}) \times a_{v_j}^{l_1}(\mathbf{k}', 0) a_{v_j}^{l_4}(-\mathbf{k}') \right], \quad (10)$$

where a_v^l (orbital index l and band index v) is the component of the eigenvectors from the diagonalization of the tight binding Hamiltonian. The orbital vertex function $\Gamma_{l_1 l_2 l_3 l_4}$ for the singlet channel and triplet channel in the fluctuation exchange

formulation[24, 38] are given by,

$$\begin{aligned} \Gamma_{l_1 l_2 l_3 l_4}^S(\mathbf{k}, \mathbf{k}', \omega) &= [\frac{3}{2} \bar{U}^s \chi_1^{RPA}(\mathbf{k} - \mathbf{k}', \omega) \bar{U}^s + \frac{1}{2} \bar{U}^s - \\ &\quad \frac{1}{2} \bar{U}^c \chi_0^{RPA}(\mathbf{k} - \mathbf{k}', \omega) \bar{U}^c + \frac{1}{2} \bar{U}^c]_{l_1 l_2 l_3 l_4}, \\ \Gamma_{l_1 l_2 l_3 l_4}^T(\mathbf{k}, \mathbf{k}', \omega) &= [-\frac{1}{2} \bar{U}^s \chi_1^{RPA}(\mathbf{k} - \mathbf{k}', \omega) \bar{U}^s + \frac{1}{2} \bar{U}^s - \\ &\quad \frac{1}{2} \bar{U}^c \chi_0^{RPA}(\mathbf{k} - \mathbf{k}', \omega) \bar{U}^c + \frac{1}{2} \bar{U}^c]_{l_1 l_2 l_3 l_4}. \end{aligned}$$

The χ_0^{RPA} describes the charge fluctuation contribution and the χ_1^{RPA} the spin fluctuation contribution. For a given gap function $g(\mathbf{k})$, the pairing strength functional is

$$\begin{aligned} \lambda[g(\mathbf{k})] &= \\ &- \frac{\sum_{ij} \oint_{C_i} \frac{dk_\parallel}{v_F(\mathbf{k})} \oint_{C_j} \frac{dk'_\parallel}{v_F(\mathbf{k}')} g(\mathbf{k}) \Gamma_{ij}(\mathbf{k}, \mathbf{k}') g(\mathbf{k}')}{4\pi^2 \sum_i \oint_{C_i} \frac{dk_\parallel}{v_F(\mathbf{k})} [g(\mathbf{k})]^2}, \end{aligned} \quad (11)$$

where $v_F(\mathbf{k}) = |\nabla_{\mathbf{k}} E_i(\mathbf{k})|$ is the Fermi velocity on a given fermi surface sheet C_i . From the stationary condition we find the following eigenvalue problem

$$-\sum_j \oint_{C_j} \frac{dk'_\parallel}{4\pi^2 v_F(\mathbf{k}')} \Gamma_{ij}(\mathbf{k}, \mathbf{k}') g_\alpha(\mathbf{k}') = \lambda_\alpha g_\alpha(\mathbf{k}), \quad (12)$$

where the interaction Γ_{ij} is the symmetric (antisymmetric) part of the full interaction in singlet (triplet) channel. The leading eigenfunction $g_\alpha(\mathbf{k})$ and eigenvalue λ_α (shown in Fig. 4c) are obtained from the above equation. The gap function has the symmetry of one of the irreducible representations for the corresponding point group.

The interaction parameters that are used in the RPA analysis, in order to avoid the magnetic instability, are systematically smaller than the FRG counterparts. Moreover, in the FRG, the bare interaction is renormalized to a smaller value as a consequence of the coupling between the particle-hole and particle-particle channels. This screening, absent in the RPA, justifies the necessity to use smaller bare interactions.

Acknowledgements. This work was supported by the DFG through SFB1170 "ToCoTronics" and by ERC-StG-336012-Thomale-TOPOLECTRICS. We gratefully acknowledge the Gauss Centre for Supercomputing e.V. (www.gauss-centre.eu) for funding this project by providing computing time on the GCS Supercomputer SuperMUC at Leibniz Supercomputing Centre (www.lrz.de).

Author contributions. R.T., W.H and D.D.S conceived the project. X.W. and D.D.S performed the DFT calculations while D.D.S, X.W. and M.F. performed the FRG calculations and many-body analysis. X.W. performed the RPA calculations. D.D.S, W.H. and R.T. wrote the manuscript and all the authors equally contributed to the scientific discussion. X.W. and D.D.S. equally contributed to the work.

Competing interests. The authors declare no competing interests.

Additional information. Correspondence and requests for materials should be addressed to D.D.S.

-
- * Electronic address: domenico.disante@physik.uni-wuerzburg.de; [†] These authors equally contributed to the work.
- [1] A. H. Castro Neto, F. Guinea, N. M. R. Peres, K. S. Novoselov, and A. K. Geim, *Rev. Mod. Phys.* **81**, 109 (2009).
- [2] A. Molle, J. Goldberger, M. Houssa, Y. Xu, S.-C. Zhang, and D. Akinwande, *Nature Materials* **16**, 163 (2017).
- [3] P. Vogt, P. De Padova, C. Quaresima, J. Avila, E. Frantzeskakis, M. C. Asensio, A. Resta, B. Ealet, and G. Le Lay, *Phys. Rev. Lett.* **108**, 155501 (2012).
- [4] A. Fleurence, R. Friedlein, T. Ozaki, H. Kawai, Y. Wang, and Y. Yamada-Takamura, *Phys. Rev. Lett.* **108**, 245501 (2012).
- [5] M. E. Dávila, L. Xian, S. Cahangirov, A. Rubio, and G. Le Lay, *New Journal of Physics* **16**, 095002 (2014).
- [6] F. d'Acapito, S. Torrengo, E. Xenogianopoulou, P. Tsipas, J. Marquez Velasco, D. Tsoutsou, and A. Dimoulas, *J. Phys. Condens. Matter* **28**, 045002 (2016).
- [7] L. Zhang, P. Bampoulis, A. N. Rudenko, Q. Yao, A. van Houselt, B. Poelsema, M. I. Katsnelson, and H. J. W. Zandvliet, *Phys. Rev. Lett.* **116**, 256804 (2016).
- [8] A. K. Geim and K. S. Novoselov, *Nature Materials* **6**, 183 (2007).
- [9] C. L. Kane and E. J. Mele, *Phys. Rev. Lett.* **95**, 226801 (2005).
- [10] F. D. M. Haldane, *Phys. Rev. Lett.* **61**, 2015 (1988).
- [11] Y. Cao, V. Fatemi, S. Fang, K. Watanabe, T. Taniguchi, E. Kaxiras, and P. Jarillo-Herrero, *Nature* **556**, 43 (2018).
- [12] I. E. Dzyaloshinskii, *Sov. Phys. JETP* **66**, 848 (1987).
- [13] R. Nandkishore, L. S. Levitov, and A. V. Chubukov, *Nature Physics* **8**, 158 (2012).
- [14] M. L. Kiesel, C. Platt, W. Hanke, D. A. Abanin, and R. Thomale, *Phys. Rev. B* **86**, 020507 (2012).
- [15] W.-S. Wang, Y.-Y. Xiang, Q.-H. Wang, F. Wang, F. Yang, and D.-H. Lee, *Phys. Rev. B* **85**, 035414 (2012).
- [16] J. L. McChesney, A. Bostwick, T. Ohta, T. Seyller, K. Horn, J. González, and E. Rotenberg, *Phys. Rev. Lett.* **104**, 136803 (2010).
- [17] C.-C. Liu, W. Feng, and Y. Yao, *Phys. Rev. Lett.* **107**, 076802 (2011).
- [18] Y. Xu, B. Yan, H.-J. Zhang, J. Wang, G. Xu, P. Tang, W. Duan, and S.-C. Zhang, *Phys. Rev. Lett.* **111**, 136804 (2013).
- [19] F. Reis, G. Li, L. Dudy, M. Bauernfeind, S. Glass, W. Hanke, R. Thomale, J. Schäfer, and R. Claessen, *Science* **357**, 287 (2017).
- [20] F.-F. Zhu, W.-J. Chen, Y. Xu, C.-L. Gao, D.-D. Guan, C.-H. Liu, D. Qian, S.-C. Zhang, and J.-F. Jia, *Nature Materials* **14**, 1020 (2015).
- [21] C.-C. Liu, H. Jiang, and Y. Yao, *Phys. Rev. B* **84**, 195430 (2011).
- [22] W. Metzner, M. Salmhofer, C. Honerkamp, V. Meden, and K. Schönhammer, *Rev. Mod. Phys.* **84**, 299 (2012).
- [23] C. Platt, W. Hanke, and R. Thomale, *Advances in Physics* **62**, 453 (2013).
- [24] N. E. Bickers, D. J. Scalapino, and S. R. White, *Phys. Rev. Lett.* **62**, 961 (1989).
- [25] T. Amlaki, M. Bokdam, and P. J. Kelly, *Phys. Rev. Lett.* **116**, 256805 (2016).
- [26] J. Reiss, D. Rohe, and W. Metzner, *Phys. Rev. B* **75**, 075110 (2007).
- [27] M. L. Kiesel, C. Platt, and R. Thomale, *Phys. Rev. Lett.* **110**, 126405 (2013).
- [28] P. M. R. Brydon, M. Daghofer, C. Timm, and J. van den Brink, *Phys. Rev. B* **83**, 060501 (2011).
- [29] C. Platt, R. Thomale, and W. Hanke, *Phys. Rev. B* **84**, 235121 (2011).
- [30] J. T. Ye, Y. J. Zhang, R. Akashi, M. S. Bahramy, R. Arita, and Y. Iwasa, *Science* **338**, 1193 (2012).
- [31] G. Kresse and J. Furthmüller, *Phys. Rev. B* **54**, 11169 (1996).
- [32] G. Kresse and D. Joubert, *Phys. Rev. B* **59**, 1758 (1999).
- [33] P. E. Blöchl, *Phys. Rev. B* **50**, 17953 (1994).
- [34] J. P. Perdew, K. Burke, and M. Ernzerhof, *Phys. Rev. Lett.* **77**, 3865 (1996).
- [35] W. Ku, T. Berlijn, and C.-C. Lee, *Phys. Rev. Lett.* **104**, 216401 (2010).
- [36] M. Tomić, H. O. Jeschke, and R. Valentí, *Phys. Rev. B* **90**, 195121 (2014).
- [37] C. Platt, R. Thomale, C. Honerkamp, S.-C. Zhang, and W. Hanke, *Phys. Rev. B* **85**, 180502 (2012).
- [38] A. F. Kemper, T. A. Maier, S. Graser, H.-P. Cheng, P. J. Hirschfeld, and D. J. Scalapino, *New Journal of Physics* **12**, 073030 (2010).
- [39] X. Wu, J. Yuan, Y. Liang, H. Fan, and J. Hu, *Europhys. Lett.* **108**, 27006 (2014).
- [40] X. Wu, F. Yang, C. Le, H. Fan, and J. Hu, *Phys. Rev. B* **92**, 104511 (2015).
- [41] C. Lu, L.-D. Zhang, X. Wu, F. Yang, and J. Hu, *Phys. Rev. B* **97**, 165110 (2018).

Supplementary Information for "Substrate-supported triplet superconductivity in Dirac semimetals"

THE TIGHT-BINDING MODEL

The eight-band tight binding model with next-nearest neighbor hopping in germanene/MoS₂ is given by

$$H_0 = \sum_{\alpha\beta} \sum_{\mu\nu\sigma} h_{\mu\nu}^{\alpha\beta}(\mathbf{k}) c_{\alpha\mu\sigma}^{\dagger}(\mathbf{k}) c_{\beta\nu\sigma}(\mathbf{k}), \quad (S1)$$

where $\alpha/\beta = A, B$ is the sublattice index and $\mu/\nu = 1, 2, 3, 4$ refer to the s, p_z, p_x and p_y orbitals, respectively. $c_{\alpha\mu\sigma}^{\dagger}$ creates a spin σ electron in μ orbital on α sublattice with momentum \mathbf{k} . The nonzero matrix elements $h_{\mu\nu}^{\alpha\beta}(\mathbf{k})$ are given by,

$$h_{11}^{AA/BB}(\mathbf{k}) = \epsilon_s + R^{11}(2\cos k_y a_0 + 4\cos \frac{\sqrt{3}}{2} k_x a_0 \cos \frac{1}{2} k_y a_0) \quad (S2)$$

$$h_{22}^{AA/BB}(\mathbf{k}) = \epsilon_{p_z} + T^{11}(2\cos k_y a_0 + 4\cos \frac{\sqrt{3}}{2} k_x a_0 \cos \frac{1}{2} k_y a_0) \quad (S3)$$

$$h_{13/31}^{AA/BB}(\mathbf{k}) = \pm 2i\sqrt{3}S_2^{12} \cos \frac{1}{2} k_y a_0 \sin \frac{\sqrt{3}}{2} k_x a_0 \quad (S4)$$

$$h_{14/41}^{AA/BB}(\mathbf{k}) = \pm 2iS_2^{12} \sin k_y a_0 \pm 2iS_2^{12} \sin \frac{1}{2} k_y a_0 \cos \frac{\sqrt{3}}{2} k_x a_0 \quad (S5)$$

$$h_{33}^{AA/BB}(\mathbf{k}) = \epsilon_{p_x} + 2T_{11}^{22} \cos(k_y a_0) + (T_{11}^{22} + 3T_{22}^{22}) \cos \frac{\sqrt{3}}{2} k_x a_0 \cos \frac{1}{2} k_y a_0 \quad (S6)$$

$$h_{44}^{AA/BB}(\mathbf{k}) = \epsilon_{p_y} + 2T_{22}^{22} \cos(k_y a_0) + (3T_{11}^{22} + T_{22}^{22}) \cos \frac{\sqrt{3}}{2} k_x a_0 \cos \frac{1}{2} k_y a_0 \quad (S7)$$

$$h_{34/43}^{AA/BB}(\mathbf{k}) = \sqrt{3}(T_{11}^{22} - T_{22}^{22}) \sin \frac{\sqrt{3}}{2} k_x a_0 \sin \frac{1}{2} k_y a_0 \quad (S8)$$

$$h_{11}^{AB}(\mathbf{k}) = r^{11}(e^{\frac{ik_x a_0}{\sqrt{3}}} + 2e^{-\frac{ik_x a_0}{2\sqrt{3}}} \cos \frac{k_y a_0}{2}) \quad (S9)$$

$$h_{22}^{AB}(\mathbf{k}) = t^{11}(e^{\frac{ik_x a_0}{\sqrt{3}}} + 2e^{-\frac{ik_x a_0}{2\sqrt{3}}} \cos \frac{k_y a_0}{2}) \quad (S10)$$

$$h_{12/21}^{AB}(\mathbf{k}) = \pm s^{11}(e^{\frac{ik_x a_0}{\sqrt{3}}} + 2e^{-\frac{ik_x a_0}{2\sqrt{3}}} \cos \frac{k_y a_0}{2}) \quad (S11)$$

$$h_{13/31}^{AB}(\mathbf{k}) = \pm [s_1^{12} e^{\frac{ik_x a_0}{\sqrt{3}}} - s_1^{12} e^{-\frac{ik_x a_0}{2\sqrt{3}}} \cos \frac{k_y a_0}{2}] \quad (S12)$$

$$h_{14/41}^{AB}(\mathbf{k}) = \pm \sqrt{3}is_1^{12} e^{-\frac{ik_x a_0}{2\sqrt{3}}} \sin \frac{k_y a_0}{2} \quad (S13)$$

$$h_{23/32}^{AB}(\mathbf{k}) = t_1^{12} e^{\frac{ik_x a_0}{\sqrt{3}}} - t_1^{12} e^{-\frac{ik_x a_0}{2\sqrt{3}}} \cos \frac{k_y a_0}{2} \quad (S14)$$

$$h_{24/42}^{AB}(\mathbf{k}) = \sqrt{3}it_1^{12} e^{-\frac{ik_x a_0}{2\sqrt{3}}} \sin \frac{k_y a_0}{2} \quad (S15)$$

$$h_{33}^{AB}(\mathbf{k}) = t_{11}^{22} e^{\frac{ik_x a_0}{\sqrt{3}}} + \frac{1}{2}(t_{11}^{22} + 3t_{22}^{22}) e^{-\frac{ik_x a_0}{2\sqrt{3}}} \cos \left(\frac{k_y a_0}{2} \right) \quad (S16)$$

$$h_{34/43}^{AB}(\mathbf{k}) = -\frac{\sqrt{3}i}{2}(t_{11}^{22} - t_{22}^{22}) e^{-\frac{ik_x a_0}{2\sqrt{3}}} \sin \left(\frac{k_y a_0}{2} \right) \quad (S17)$$

$$h_{44}^{AB}(\mathbf{k}) = t_{22}^{22} e^{\frac{ik_x a_0}{\sqrt{3}}} + \frac{1}{2}(3t_{11}^{22} + t_{22}^{22}) e^{-\frac{ik_x a_0}{2\sqrt{3}}} \cos \left(\frac{k_y a_0}{2} \right) \quad (S18)$$

where a_0 is the inplane lattice constant, $r(R)$ represents hopping between s and s orbitals for the nearest neighbors (next nearest neighbors), $t(T)$ represents hopping between p and p orbitals for the NN (NNN) and $s(S)$ represents hopping between s and p orbitals for the NN (NNN). The hopping parameters in the model are

$$r^{11} = V_{ss\sigma}, t^{11} = \cos^2 \theta V_{pp\sigma} + \sin^2 \theta V_{pp\pi}, s_1^{12} = \sin \theta V_{sp\sigma}, s_1^{11} = \cos \theta V_{sp\sigma}, \quad (S19)$$

$$t_1^{12} = -\cos \theta \sin \theta (V_{pp\pi} - V_{pp\sigma}), t_{11}^{22} = \sin^2 \theta V_{pp\sigma} + \cos^2 \theta V_{pp\pi}, t_{22}^{22} = V_{pp\pi}, \quad (S20)$$

$$R^{11} = V'_{ss\sigma}, S_2^{12} = V'_{sp\sigma}, T^{11} = T_{11}^{22} = V'_{pp\pi}, T_{22}^{22} = V'_{pp\sigma}. \quad (S21)$$

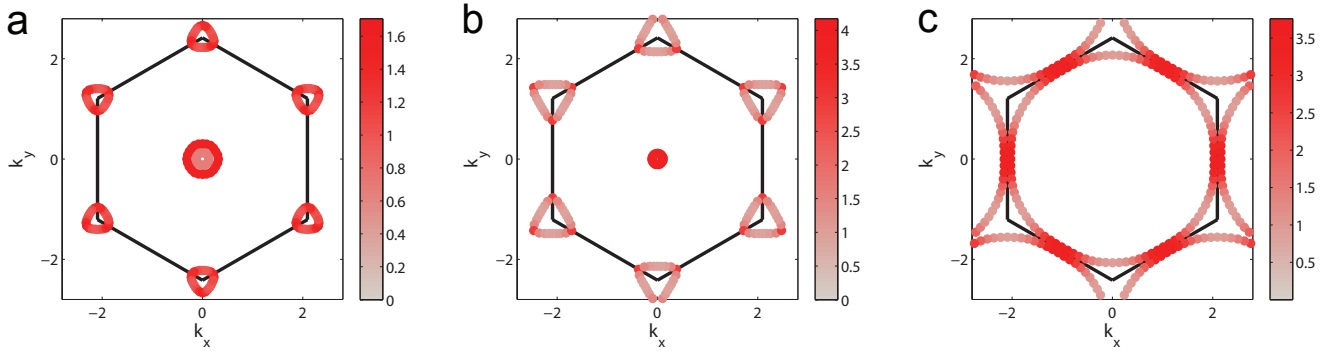


FIG. S1: Distribution of the momentum resolved DOS along the Fermi surface at half-filling (a), 0.08 electron doping (b) and at the vHs (c).

The corresponding parameters (in eV) in the calculations are

$$\epsilon_s = -7.0238, \epsilon_{p_x}/p_y = 1.3088, \epsilon_{p_z} = 1.9777, \theta = 111.44^\circ \quad (S22)$$

$$V_{ss\sigma} = -1.3610, V_{sp\sigma} = 1.7288, V_{pp\sigma} = 3.0701, V_{pp\pi} = -0.6206, \quad (S23)$$

$$V'_{ss\sigma} = -0.0729, V'_{sp\sigma} = 0.3184, V'_{pp\pi} = -0.1081, V'_{pp\sigma} = 0.6999. \quad (S24)$$

TRIPLET PARING FROM THE ANALYSIS OF THE FERMI VELOCITY

The density of states generally can be written as $\rho(E) = \frac{\Omega}{(2\pi)^3} \sum_n \int d\mathbf{k} \delta(E - \epsilon_{n\mathbf{k}})$. We rewrite $d\mathbf{k}$ as $dS_{\parallel} dk_{\perp}$, where k_{\perp} is along the gradient direction of $\epsilon_{n\mathbf{k}}$ and dS_{\parallel} is the infinitesimal area of the iso-energy surface. Using $d\epsilon = |\nabla_{\mathbf{k}} \epsilon_{n\mathbf{k}}| dk_{\perp}$, we can obtain $\rho(E) = \frac{\Omega}{(2\pi)^3} \sum_n \int dS_{\parallel} \frac{1}{|\nabla_{\mathbf{k}} \epsilon_{n\mathbf{k}}|}$. When $|\nabla_{\mathbf{k}} \epsilon_{n\mathbf{k}}| = 0$ at some \mathbf{k} point, it is a saddle point and called van Hove singularity point. At the Fermi level, the density of state for the \mathbf{k} points on surfaces is $\rho(E_f, \mathbf{k}_F) \sim \frac{1}{|\nabla_{\mathbf{k}} \epsilon_{n\mathbf{k}}|} = \frac{1}{|v_F(\mathbf{k}_F)|}$. The \mathbf{k} point with smaller Fermi velocity will contribute more to the DOS.

For the case of germanene within the DFT Wannier model, the inverse of the Fermi velocity is given in Fig. S1 for three different doping values. At the vHs we find that not only \mathbf{k} -points around M but also along the M-K direction are characterized by a very small Fermi velocity, indicating that all these points give a considerable contribution to the DOS. This is quite different, for example, from the simple graphene model with NN hopping. The analytical RG method used by Nandkishore et al. in Nat. Phys. **8** 158 (2012), where only the three M points are considered, is not applicable. In germanene on MoS₂, the description is very similar to the case of type-II vHs points (the saddle points are not at the time reversal invariant points). The saddle points contribute dominantly to DOS and enhance the ferromagnetic fluctuations, which can promote triplet pairing. The triplet pairing at the standard type-I vHs (saddle points at time reversal invariant momenta) is forbidden because of the Pauli exclusion principle.

THE INFLUENCE OF THE BUCKLING IN GERMANENE

For freestanding germanene, the lattice constant is $a = 4.06\text{\AA}$ and the buckling is about 0.7\AA ($\theta = 106^\circ$). When germanene is grown on MoS₂, the lattice constant reduces to $a = 3.82\text{\AA}$ and the buckling is 0.86\AA ($\theta = 111.4^\circ$) due to strain effects from the substrate. In this specific case, the coupling between germanene and MoS₂ is weak and the most important effect is the strain. Fig. S4a shows the band structures for germanene with different bucklings (different lattice constants), where the pink line denotes the band structure for freestanding germanene. By increasing the buckling, the $p_{x,y}$ band at Γ point moves up, the VHS at M moves down and the band around the vHs becomes flatter. When the buckling is larger than 0.86\AA , the $p_{x,y}$ band is above the vHs point at half-filling and we realize a compensated semimetal phase, where there are both electron and hole pockets at the vHs. The buckling angle θ increases with increasing the buckling and it affects the hopping amplitude between the A and B sublattices. The Fermi surfaces for freestanding germanene and germanene/MoS₂ are shown in Fig. S4b,c. We find that the Fermi surface for the larger buckling is flatter near the M point. How to understand the effect of the buckling on the band structures from a microscopic viewpoint? By increasing θ , the coupling between p_z orbitals (t^{11}) and the coupling between $p_{x,y}$ orbitals (t_{11}^{22}, t_{22}^{22}) will decrease (see equations in the tight-binding model of the Methods Section). At the Γ point, the $p_{x,y}$ bands

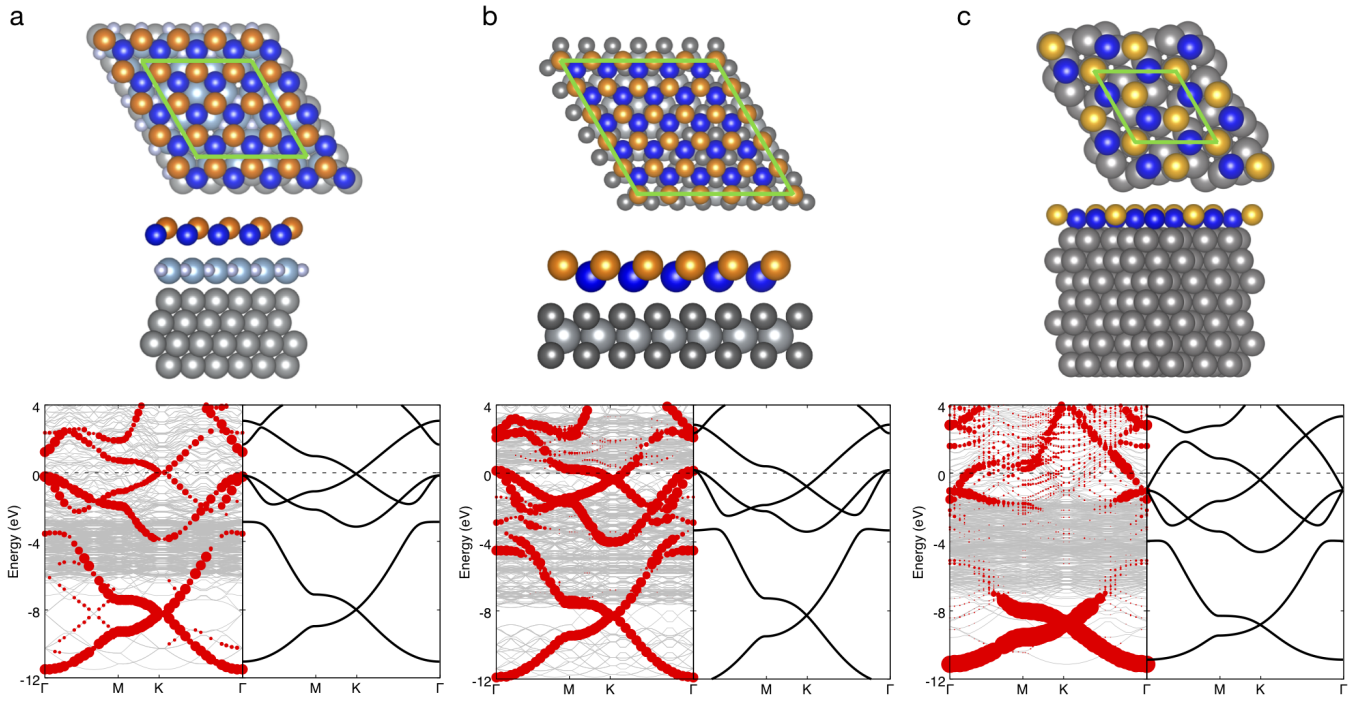


FIG. S2: First-principles calculations of realistic germanene's models. **a** 3×3 germanene on 4×4 AlN/Ag(111), **b** 5×5 germanene on 6×6 MoS₂ and **c** $\sqrt{3} \times \sqrt{3}R(30^\circ)$ germanene on $\sqrt{7} \times \sqrt{7}R(19.1^\circ)$ Au(111). In the top and side views the orange and blue spheres refer to protruding and low Ge atoms, respectively. The unit cell for the three germanene's reconstructions that we considered here is in light green. The lower panels show the DFT bandstructures for each supercell along the high-symmetry-lines of the 1×1 Brillouin zones (grey lines). The red circles highlight the weights of the unfolded electronic states. In black solid lines, the bandstructures of the nearest neighbour 8-bands Slater-Koster model with parameters listed in Table (I).

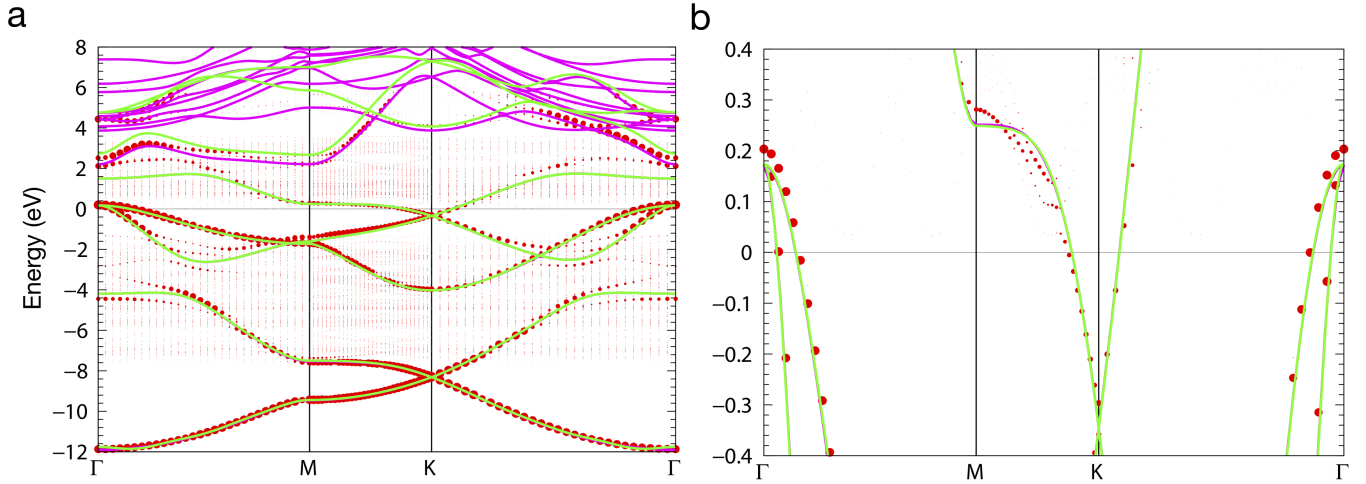


FIG. S3: Large energy view and zoom of the comparison between the bandstructures of germanene/MoS₂ (DFT), monolayer germanene (DFT) and Wannier functions based Hamiltonian with D_{3d} symmetry (used as the non interacting reference for our FRG and RPA calculations).

are the bonding states between the A and B sublattice and therefore they move up when the corresponding coupling decreases. The decrease of $|t^{11}|$ leads to the downward shift of the vHs at the M point.

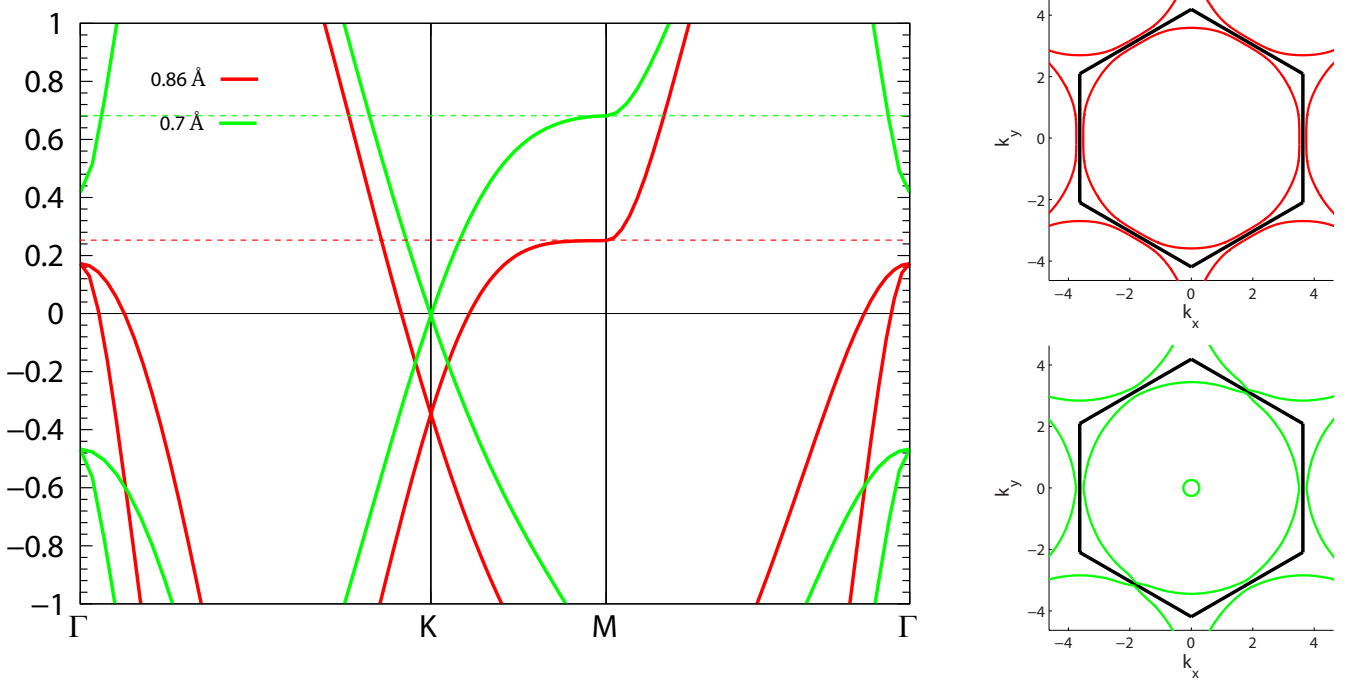


FIG. S4: **left** Bandstructures for germanene with different buckling values (and relative different lattice constants). The green and red lines denote the bandstructures for freestanding germanene and germanene/MoS₂, respectively. **right** Fermi surfaces at the vHs for freestanding germanene (0.7 Å) and germanene/MoS₂ (0.86 Å).